Journal of Biomechanics 123 (2021) 110504

Contents lists available at ScienceDirect

Journal of Biomechanics

journal homepage: www.elsevier.com/locate/jbiomech
www.JBiomech.com

Topographic features of nano-pores within the osteochondral interface and their effects on transport properties –a 3D imaging and modeling study

Behdad Pouran [a,h,*], Amir Raoof [c], D.A. Matthijs de Winter [a,d], Vahid Arbabi [a,j], Ronald L.A.W. Bleys [e], Frederik J. Beekman [g,h,i], Amir. A. Zadpoor [b], Jos Malda [a,f], Harrie Weinans [a,b]

[a] Department of Orthopaedics, University Medical Centre Utrecht, Utrecht, the Netherlands
[b] Department of Biomechanical Engineering, Faculty of Mechanical, Maritime and Materials Engineering, Delft University of Technology, Delft, the Netherlands
[c] Hydrogeology, Faculty of Geosciences, Utrecht University, Utrecht, the Netherlands
[d] Wetsus, Centre of Excellence for Sustainable Water Technology, Leeuwarden, the Netherlands
[e] Department of Anatomy, University Medical Centre Utrecht, Utrecht, the Netherlands
[f] Department of Equine Sciences, Utrecht University, Utrecht, the Netherlands
[g] Section Radiation, Detection & Medical Imaging, TU-Delft, the Netherlands
[h] MILabs, Utrecht, the Netherlands
[i] Dept. of Translational Neurosciences, University Medical Centre Utrecht, Utrecht, the Netherlands
[j] Orthopaedic-BioMechanics Research Group, Department of Mechanical Engineering, University of Birjand, Birjand, Iran

ARTICLE INFO

Article history:
Accepted 2 May 2021

Keywords:
Osteochondral junction
Solute transport
Permeability
Nanopore architecture
Pore -scale modelling

ABSTRACT

Recent insights suggest that the osteochondral interface plays a central role in maintaining healthy articulating joints. Uncovering the underlying transport mechanisms is key to the understanding of the cross-talk between articular cartilage and subchondral bone. Here, we describe the mechanisms that facilitate transport at the osteochondral interface. Using scanning electron microscopy (SEM), we found a continuous transition of mineralization architecture from the non-calcified cartilage towards the calcified cartilage. This refurbishes the classical picture of the so-called tidemark; a well-defined discontinuity at the osteochondral interface.

Using focused-ion-beam SEM (FIB-SEM) on one osteochondral plug derived from a human cadaveric knee, we elucidated that the pore structure gradually varies from the calcified cartilage towards the subchondral bone plate. We identified nano-pores with radius of 10.71 ± 6.45 nm in calcified cartilage to 39.1 ± 26.17 nm in the subchondral bone plate.

The extracted pore sizes were used to construct 3D pore-scale numerical models to explore the effect of pore sizes and connectivity among different pores. Results indicated that connectivity of nano-pores in calcified cartilage is highly compromised compared to the subchondral bone plate. Flow simulations showed a permeability decrease by about 2000-fold and solute transport simulations using a tracer (iodixanol, 1.5 kDa with a free diffusivity of 2.5×10^{-10} m^2/s) showed diffusivity decrease by a factor of 1.5. Taken together, architecture of the nano-pores and the complex mineralization pattern in the osteochondral interface considerably impacts the cross-talk between cartilage and bone.

© 2021 The Author(s). Published by Elsevier Ltd. This is an open access article under the CC BY license (http://creativecommons.org/licenses/by/4.0/).

1. Introduction

The osteochondral interface bridges the articular cartilage to the subchondral bone plate and balances the un-matching mechanical properties of non-calcified soft cartilage and the stiff subchondral bone plate. Our previous experimental observations, in conjunction with other studies, confirmed the transport of solutes across the osteochondral interface (Burstein et al., 2001; Pan et al., 2012; Pan et al., 2009; Pouran et al., 2016a). This factor may play a role in the cross-talk between cartilage and bone and highlights a possible signal transduction mechanism in articulating joints involved in the development and recovery processes of cartilage and related diseases, such as osteoarthritis (Pan et al., 2009; Weinans et al., 2012).

* Corresponding author at: Department of Orthopaedics, University Medical Centre Utrecht, Utrecht, the Netherlands.
E-mail address: b.pouran@umcutrecht.nl (B. Pouran).

https://doi.org/10.1016/j.jbiomech.2021.110504
0021-9290/© 2021 The Author(s). Published by Elsevier Ltd.
This is an open access article under the CC BY license (http://creativecommons.org/licenses/by/4.0/).

A large amount of studies has focused on solute transport across articular cartilage, since it is vital for the many biological activities of chondrocytes (Quinn et al., 2001). For instance, static compression has been shown to decrease solute transport of small and large solutes across articular cartilage (Quinn et al., 2001). Load-dependent fluid flow has been also shown to affect water, solute and mechanical properties of articular cartilage (Mow et al., 1984; Torzilli et al., 1983). Alterations of extracellular matrix affects the way solutes interact with the matrix and subsequently alters the transport: mechanically injured cartilage explants increased diffusivity (Chin et al., 2013). It has been shown that the diffusivity decreases with solute size and importance of the negative charges of proteoglycans particularly on the transport of charged solutes has been emphasized (Arbabi et al., 2016a; Bajpayee et al., 2014; Leddy and Guilak, 2003; Pouran et al., 2018; Pouran et al., 2016b; Torzilli et al., 1987). Means for the solute and fluid transport in cortical bone have been investigated as well and were attributed to an interconnected pore network within the lacunar-canalicular region (Benalla et al., 2014; Wang et al., 2000). The existence and the exact role of porosity inside the deep cartilage layers, the extracellular matrix of calcified cartilage and subchondral bone plate have not been fully clarified.

Therefore, in this study, we evaluated the topographic features of nano-pores within the osteochondral interface both in relatively healthy and more degenerated tissue. For this, we performed micro-computed tomography (micro-CT)-based inspection of human osteochondral plugs from three donors. Ultramicrotome-cut sections of 10 μm thick were used either for histology or FIB-SEM. The FIB-SEM observations of the sections were correlated to the histology staining to verify the location of the calcified cartilage and the subchondral bone.

2. Materials and methods

2.1. Sample harvest

Four osteochondral plugs (diameter = 8.5 mm) were harvested from two human cadaveric femoral condyles. They included two osteochondral plugs per condyle from the regions with minimum visually detectable cartilage damage (donor age between 75 and 88), using a custom-made drill bit (Arbabi et al., 2017). The drilling was performed while continuously spraying the drilling site using phosphate buffer solution (PBS) enriched with protease inhibitor (cOmplete, Germany). The osteochondral plugs were put in a plastic vial. The vials were placed in a container which was sealed in a bag and stored at −20 °C.

2.2. Micro-computed tomography (micro-CT)

The osteochondral plugs were scanned with a micro-CT (U-CT^{UHR}, MILabs B.V., The Netherlands) at a resolution of 15 μm FWHM with a tube voltage of 60 kV and tube current of 200 μA. The scans were then reconstructed with a Feldkamp (FDK) algorithm with correction for beam hardening, a Hann pre-filter and a 3D Gaussian post-filter to enable to quantify the grey values at the osteochondral interface.

2.3. Cryo-sectioning

Post-micro-CT, the osteochondral plugs were embedded in an resin (Cryo-Gel, Leica) within the chamber of cryo-microtome (Leica CM3600 XP, Germany, −25 °C) and serial sectioning (alternating sections for FIB-SEM and histology) was performed perpendicular to the interface of cartilage and bone. The sections (10 μm) were collected on coated glass slides (SuperfrostTM Plus, Thermo-Fisher). After immersion in ethanol series (100%, 90%, 70%) for five minutes, the sections were incubated for 45 min in the oven at 60 °C to ensure stable attachment of the sections to the glass slide surface.

2.4. Histology

To locate the calcified cartilage and subchondral bone plate within the slides and to assess the healthiness of the osteochondral plugs, Safranin-O/Fast green staining was performed to a number of sections that would not undergo FIB/SEM.

2.5. Focused-ion-beam scanning electron microscopy (FIB/SEM)

After freeze-drying (Christ alpha 1–2 LD plus) the sections for 24 h, Glass slides containing one or more sections were attached to a standard SEM aluminium stubs with adhesive carbon tape. A small strip of the tape was stuck to the edge of the section and led to the SEM stub to improve electrical conductivity. Subsequently, the glass slide was sputter coated with 5 nm Pt/Pd (Cressington 208HR). FIB-SEM operations were performed on a Helios Nanolab UC-G3 (FEI). A small strip of Pt deposition was deposited from the bone region to the uncalcified cartilage region (thickness approximately 1 μm). Subsequent FIB milling (30 kV, stepwise reducing the ion current from 21 nA – 24 pA) resulted in a wide cross section. Backscatter Electron (BSE) imaging (2 kV, 0.2 nA) with the through the lens detector in immersion mode revealed the pore structure.

FIB-SEM tomography (WINTER et al., 2009) was performed with Slice & View™ G3 v1.7.3 (FEI). Slices of 20 nm were milled with 30 kV, 24 pA and imaged in BSE mode (2 kV, 0.2 nA) with the through the lens detector in immersion mode.

2.6. Pore-scale modelling

The FIB-SEM tomography data was further analysed using ImageJ. The pore space was segmented, resulting in binary data (pore space versus solid). Subsequently, the pore space was converted into a network of pores for modelling as a system of pore junctions connected by pore segments (Fig. M1).

We chose the pore network method (using PoreFlow package, (Raoof et al., 2013)) for our permeability simulations. This method provides computational efficiency where fluid flow and reactive solute transport in three dimensions can be simulated in very large number of pores. The accuracy of the numerical schemes available in PoreFlow has been tested against several experimental observations (e.g., (Mahmoodlu et al., 2020)). Through image analysis, each pore segment obtains a hydraulic conductance depending on its size and length. We focused on exploring the permeability of the imaged pore structure, neglecting the possible geometry change (e.g., due to compression). Compression effects can be considered by coupling pore network modeling with the Discrete Element

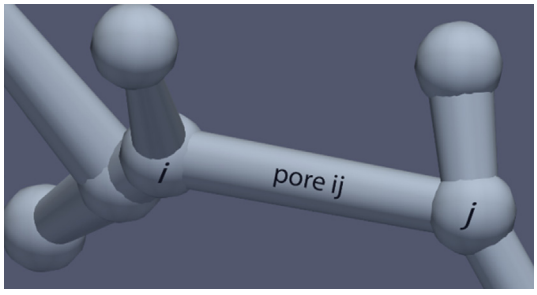

Fig. M1. An example of interconnected pore, ij, and junctions, i and j, obtained from the bone sample.

Method (DEM) modeling (e.g., in (Mahmoodlu et al., 2016)). However, given the focus and size of this study, we have chosen not to include mechanical effects, as this would require exploring a separate set of parameters.

The resulting flow through a particular pore segment is calculated using the following relationship:

$$q_{ij} = \frac{\pi R_{ij}^4}{8\mu l_{ij}}(P_j - P_i) \tag{1}$$

where *qij* is volumetric flow through a given pore segment *ij*, R_{ij} and l_{ij} are the radius and length of pore throat, respectively. μ is dynamic viscosity, *Pi* and *Pj* are pressures at pore junctions *i* and *j*, respectively. Eq. (1) can be defined for each and every pore segment together.

Solute transport across the pore segment can be calculated by solving mass balance Eq. (2) which describes change of concentration for a given pore, c_{ij}, as a result of both advection and diffusion transport processes.

$$V_{ij}\frac{dc_{ij}}{dt} = \underbrace{q_{ij}\left(c_j^{-t+\Delta t} - c_{ij}^{-t+\Delta t}\right)}_{\text{advection process}} + DA_{ij}\frac{\left(c_j^{-t+\Delta t} - c_{ij}^{-t+\Delta t}\right)}{l_{ij}} + \underbrace{DA_{ij}\frac{\left(c_i^{-t+\Delta t} - c_{ij}^{-t+\Delta t}\right)}{l_{ij}}}_{\text{diffusion process}} \tag{2}$$

where V_{ij} *and* A_{ij} are volume and pore cross-sectional area respectively, c_{ij} and c_i are concentrations belonging to the upstream pore junction *i* and pore *ij* itself and *D* is molecular diffusion.

Another mass balance equation is written for each pore junction, c_i, where solutes from connected pores to it may exchange mass:

$$V_i\frac{dc_i}{dt} = \underbrace{\sum_{j=1}^{j=z_{i,\text{inflow}}} q_j c_j^{-t+\Delta t} - Q_i c_i^{-t+\Delta t}}_{\text{advection process}} + \underbrace{\sum_{j=1}^{Z_i} DA_{ij}\frac{c_j^{-t+\Delta t} - c_i^{-t+\Delta t}}{l}}_{\text{diffusion process}}, \tag{3}$$

$$\text{Where } \sum_{j=1}^{j=z_{i,\text{inflow}}} q_j = Q_i = \text{total flux}$$

where *Vi* is the pore junction volume and z_i is the pore connectivity, showing the number of pores connected at the junction *i*.

Finally, the overall solute transport can be determined for a given concentration gradient across the pore space by solving Eq. (2) and Eq. (3) for all pore segments and pore volumes using a fully implicit method, which converges to a stable concentration distribution across the pore space. The time step for each time step is determined by:

$$\Delta t \le min\left\{\frac{l^2}{4D_{diff}}\right\} \tag{4}$$

To characterize diffusion behaviour, a dimensionless transport hindrance coefficient, τ [-], is defined as the ratio of calculated diffusivity ($D_{Calculated}$) through the real pore network to the diffusivity ($D_{Unhindered}$) through a straight opening across the same length and with the same porosity:

$$\tau = D_{Calculated}/\ D_{Unhindered} \tag{5}$$

To allow comparisons with the previous studies, iodixanol (1.5 kDa) with a free diffusivity of 2.5 × 10–10 m^2/s was modelled.

3. Results and discussion

3.1. 2D nano-topography and mineralization

Cross sections were obtained using FIB-SEM, which revealed the presence of a nano-porosity region across the entire osteochondral interface (Figs. 1 and 2). Mineralization is seen on the SEM images as white pixels, compared to black pixels corresponding to regions with no mineralization. Using imageJ, the mineralized region was thresholded and its percentage was calculated by dividing the area of the mineralized region by the total area. The images demonstrate gradual transition in the extent of mineralization (white regions) between the non-calcified cartilage (~11% mineral) and the deeper zones of calcified cartilage close to the subchondral bone (~97% mineral) (Region 1, Fig. 2). This observation

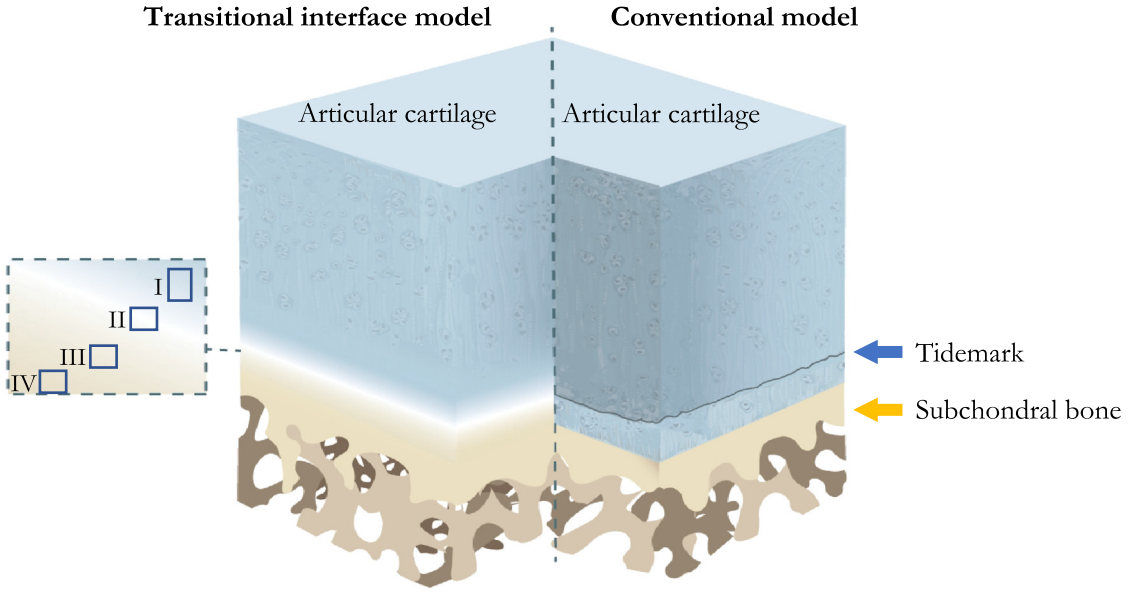

Fig. 1. Transitional interface model of the cartilage-bone interface versus conventional model. Contrary to strict separation between uncalcified cartilage, calcified cartilage and subchondral bone plate in the conventional model, transitional model introduces the concept of continuous interfaces based on the findings of focused-ion-beam scanning electron microscopy (FIB-SEM). Four different zones are introduced at the cartilage-bone interface: Region I starts in the deep uncalcified cartilage and proceeds into the fully calcified region. Regions II, III and IV are located in the calcified cartilage (near the uncalcified cartilage), calcified cartilage (near the subchondral bone plate) and in the subchondral bone plate, respectively.

complements the classical cartilage model (Hughes et al., 2005; Sophia Fox et al., 2009), describing a sharp and undulating finite-size interface which features high calcium content.

The fact that mineralization increases rapidly at once, transiting from non-calcified cartilage to calcified cartilage, has been reflected using Fourier transform infrared imaging (Khanarian et al., 2014). However, the maximum resolution of few microns using that technique did not allow detecting individual nano-sized features at the interfaces. Using FIB-SEM, we observed that the calcified cartilage contains segregated non-mineralized regions near the non-calcified cartilage, which enhances transport of solutes due to the presence of gel-like material comprising of water, collagen and glycosaminoglycans (Region I, Fig. 2) (Sophia Fox et al., 2009). We also confirmed that the topographic transition between calcified cartilage and subchondral bone is gradual (Figs. 1 and 2).

3.2. 3D micro- and nano-topography and pore size distribution

Calcified cartilage in the relatively healthy sample (normal cartilage surface with less surface fibrillation) develops larger and more dispersed pores in comparison to the degenerate sample (Regions 2 and 3, Fig. 2). This observation is verified by the grey values from the micro-CT showing a thicker layer of calcified cartilage in the degenerate sample compared to the healthy sample (Figure S1). Near the subchondral bone plate region, the pores become larger where they reach the maximum size within the bone region (Region IV, Figs. 1 and 2).

To capture the sub-micrometre porous structure of the calcified cartilage and subchondral bone plate, we employed a focused ion beam-scanning electron microscope (FIB-SEM tomography). Doing so, site-specific cross-sections can be directly imaged at a nanometre resolution using SEM. The successive FIB cross-sectioning and SEM imaging during the FIB-SEM tomography provide three-dimensional volumetric representations with nanometre resolution across the micrometre length scales (de Winter et al., 2016; Narayan and Subramaniam, 2015; WINTER et al., 2009). The FIB-SEM tomography-based 3D reconstruction of the pore space in the healthier sample led to the characterization of the pore structures within the calcified cartilage and subchondral bone plate. The analysed 3D volumes were 10 μm × 4 μm × 2.5 μm for the calcified cartilage (regions II and III, Fig. 2) and 4 μm × 4 μm × 3 μm for the subchondral bone plate.

The porosity of the calcified cartilage and subchondral bone plate (region IV, Fig. 2) were found to be 1.6% and 9.7%, respectively. The average pore diameter of the extracellular matrix of calcified cartilage (i.e. non-mineralized collagen fibrils) was 10.71 ± 6.45 nm, considerably smaller than that of the subchondral bone plate (canalicular space and non-mineralized collagen fibrils) with a value of 39.1 ± 26.17 nm (Fig. 3, and Region IV in Fig. 2)). Therefore, the calcified cartilage would naturally block solutes larger than 10 nm in diameter. However, our findings confirm the pres-

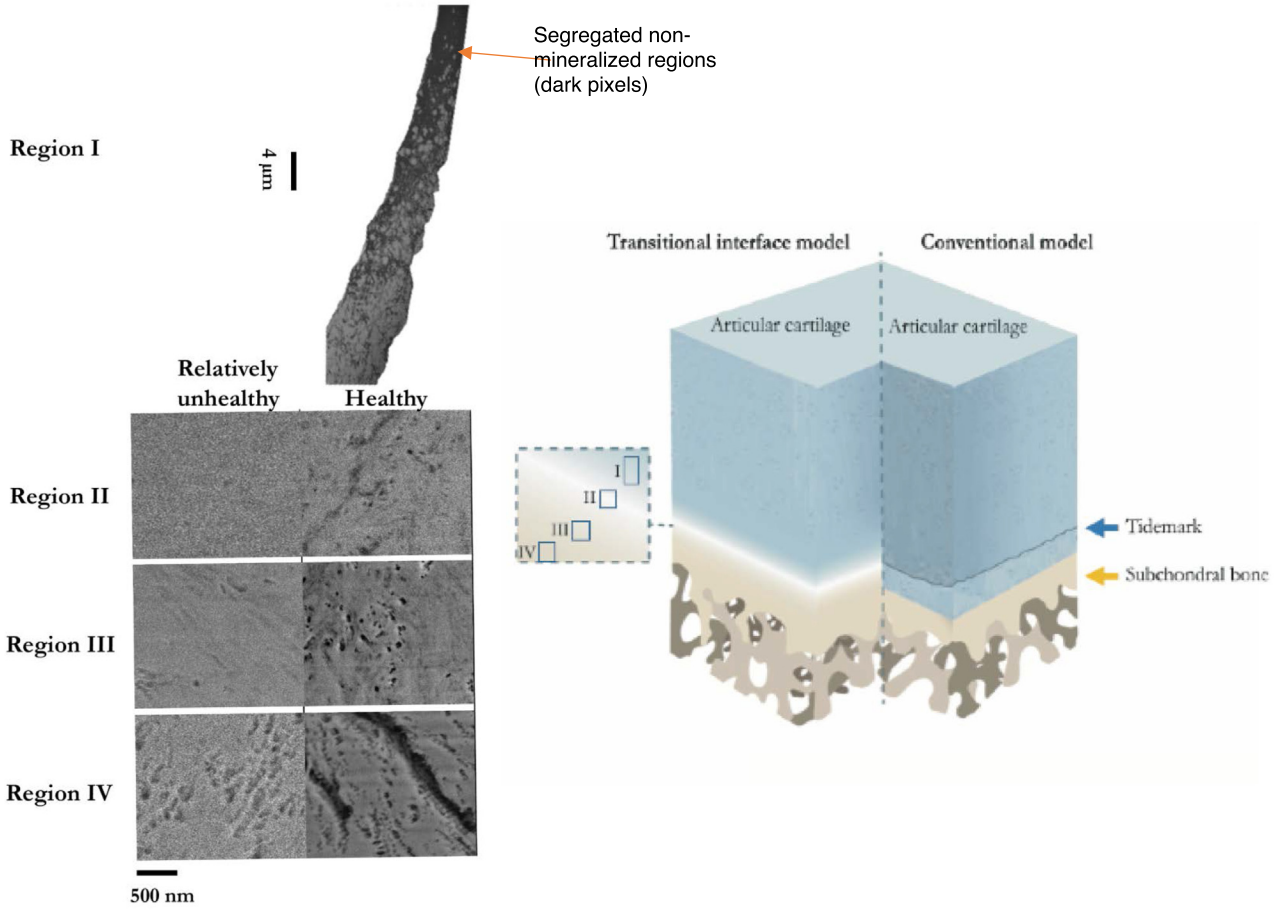

Fig. 2. Nano-topographic features of regions I, II, III and IV (Fig. 1)- introduced by transitional interface model - obtained using scanning electron microscopy. Continuous increase in mineralization while proceeding from non-calcified cartilage to the calcified cartilage (Region 1, white pixels demonstrate the mineralized material, whereas dark pixels demonstrate the non-mineralized materials). Regardless of the degree of healthiness, pores increase in size by transitioning towards subchondral bone plate (Regions II, III and IV). Region II represents the matrix of calcified cartilage depicting highly dense mineralized material. The pores in the calcified cartilage originate from the partial mineralization of collagen fibrils. Region IV located in the subchondral bone plate shows maximal pore size with abundance of pores.

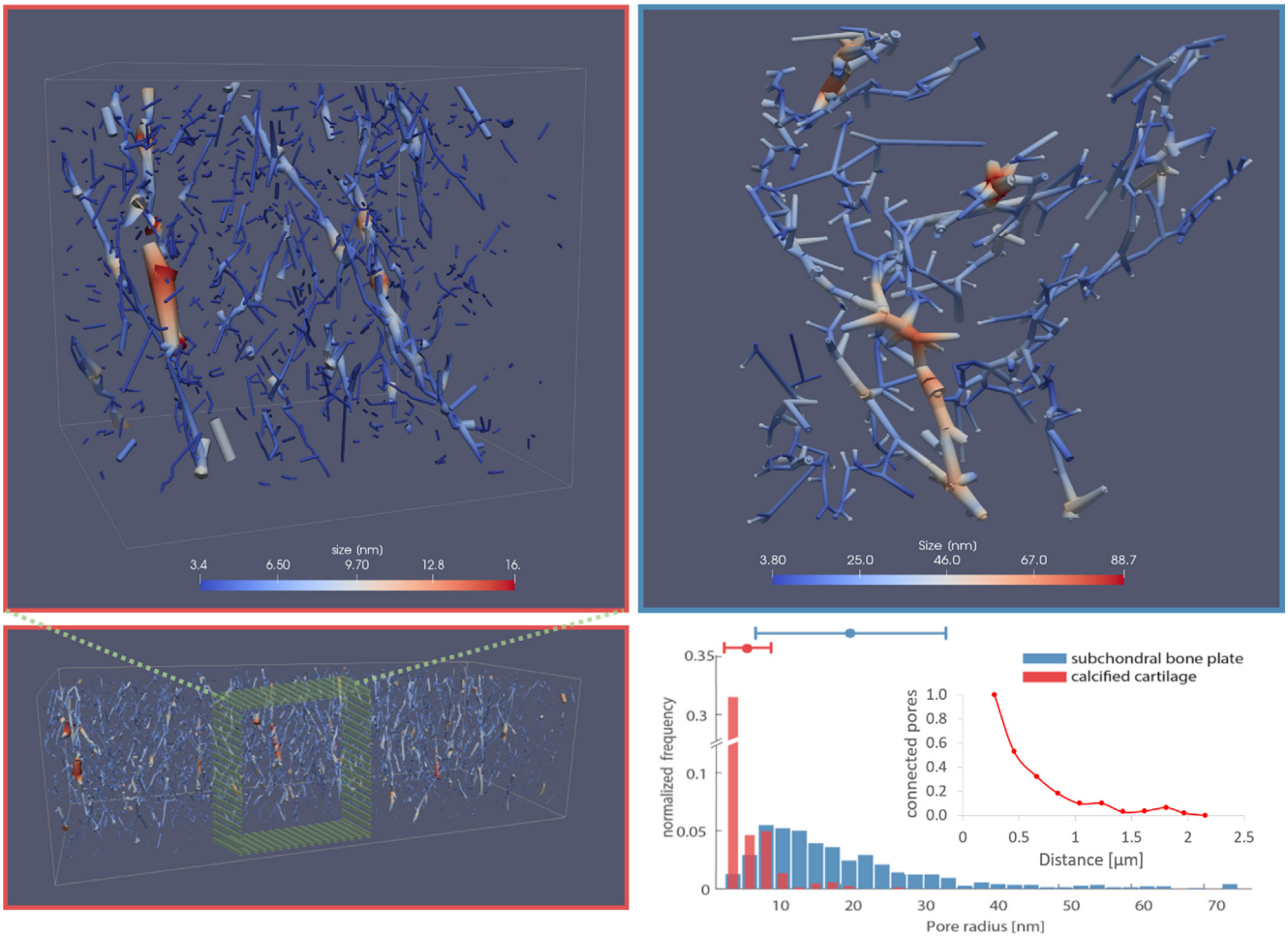

Fig. 3. 3D pore structure with the size in color of calcified cartilage (left) and subchondral bone plate (right). The pores in calcified cartilage are smaller and less frequently connected compared to those of subchondral bone plate. Pore size distribution for calcified cartilage and subchondral bone plate is plotted separately confirming the visual observations.

ence of pore spaces in the calcified cartilage, even in the almost completely calcified region near the subchondral bone plate (regions II and III in Fig. 2).

3.3. Pore interconnectivity and length-dependent diffusion

The 3D-reconstructed pore spaces were used for pore interconnectivity analysis and for computational flow and solute transport simulations to obtain the diffusivity and permeability values. The 3D-reconstructed pore spaces show that the interconnectivity of pore networks within calcified cartilage decreases as a function of length (Fig. 3). This provides a key finding that the diffusion across the osteochondral interface is length dependent and vanishes at the larger thicknesses of the calcified cartilage due to scarcity of the connected pores.

The length dependency of diffusion process was explored by obtaining solute concentration versus time curves (i.e., solute concentration arrivals) at several locations with increasing distances along the subchondral bone plate (Fig. 4A). As the diffusive flux is governed by the Fick's law and is linear in nature (Eq. (2)), the transport metrics corresponding to other diffusivities or other concentrations over the boundaries can be calculated using the ratio of the desired diffusivities or boundary concentrations to their corresponding values applied in this study. Previously reported diffusivities in the calcified cartilage of mice, between the chondrocytes, were much lower than our diffusivity values (Pan et al., 2009). These values were obtained merely in the region of calcified cartilage close to non-calcified cartilage where non-mineralized patches may facilitate the transport. The justification for the variations between the values reported earlier and here mainly originates from the length-scale differences (Table 1); our results have been obtained within the pore domain, whereas the previously obtained results have been derived from larger continuum scale formulations (the so-called tissue level) (Arbabi et al., 2016b; Pan et al., 2012; Pan et al., 2009).

The pore-scale diffusivity in the subchondral bone plate can be 16-fold higher than that in the tissue level, which is consistent with the earlier study (Fan et al., 2016). Higher diffusivities at the pore-scale are attributed to the higher freedom of solutes to distribute, as they do not encounter the highly impermeable solid mineralized phase. Furthermore, pore-scale analysis allows exact determination of diffusivity in subchondral bone plate and calcified cartilage separately, as opposed to contrast-enhanced micro-CT which cannot discriminate between these two mineralized compartments. It is important to note that the computed values here were obtained at the extracellular matrix region, as the added cellular space would potentially affect those.

3.4. Quantifying the anisotropy behaviour of diffusion

In calcified cartilage and parallel to the osteochondral interface, transport hindrance coefficient (τ) decreased from 0.16 at a loca-

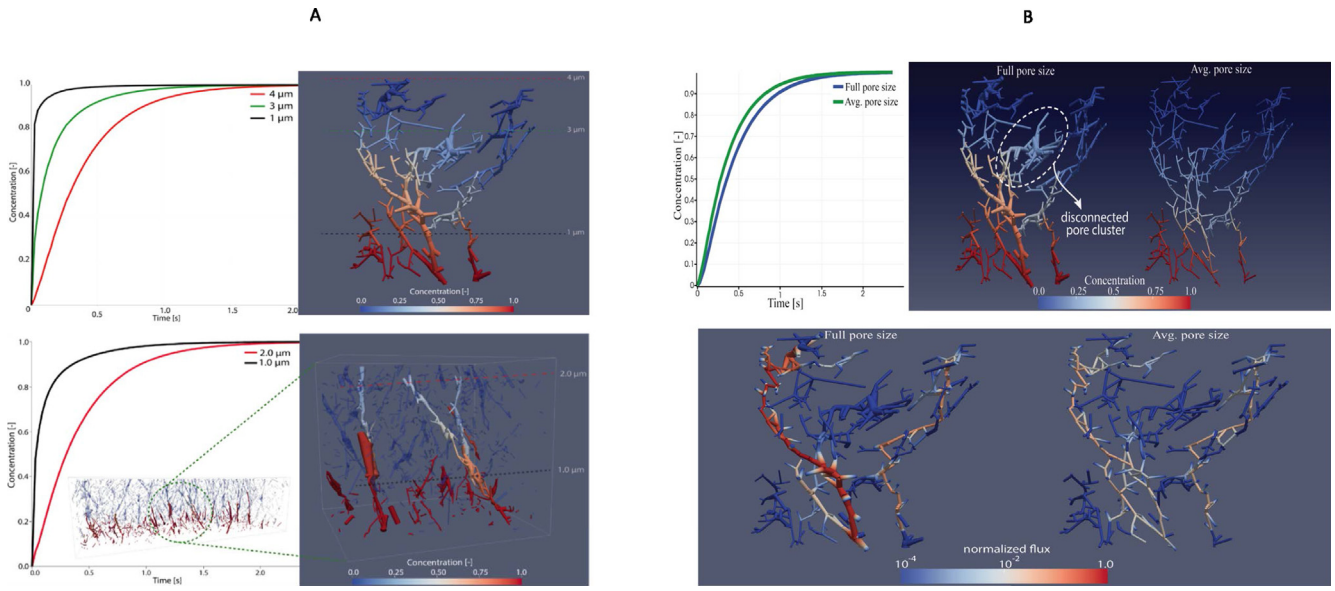

Fig. 4. A) Top: Normalized concentration vs. time in different length scales perpendicular to the osteochondral interface for subchondral bone plate. Bottom: Normalized concentration vs. time in different length scales parallel to the osteochondral interface for calcified cartilage. Solute free diffusivity value is equal to 2.5×10^{-10} m^2/s for all simulations. B) Top: Time arrival of solute concentration for two pore structures within bone. Right image: pore structure with real pore size distribution, and the pore structure with pores having the average size. Bottom: Flux of fluid for real pore size distribution (left plot), and the pore structure with pores having the average size (right plot). The flux values are normalized using the maximum flux value. Although the pore network with the uniform pore size shows similar domain flow pathway as that of the real pore network, its magnitude is considerably weaker (as shown by the lighter red colour). (For interpretation of the references to color in this figure legend, the reader is referred to the web version of this article.)

tion of half of the 3D FIB-SEM sample size (i.e., at 1 μm) to 0.13 for the entire 3D FIB-SEM volume (2 μm), showing diffusivity decrease with length.

In contrast to the above, τ value in calcified cartilage was found to be 0.05 in direction perpendicular to the osteochondral interface (with 0.7 μm). Therefore, calcified cartilage is more conductive in the direction parallel to osteochondral interface. Such a pronounced anisotropy in diffusivity indicates that the calcified cartilage mainly acts as a solute distributor in its entire volume rather than enhancing passage of solutes towards the subchondral bone plate. Previous research found local pathways across the interface where non-calcified cartilage meets the subchondral bone plate (Lyons et al., 2006), suggesting that the solutes preserved in the matrix of (calcified) cartilage can become available at the subchondral bone plate.

In the subchondral bone plate, parallel to osteochondral interface, τ was found to be 0.21. Perpendicular to osteochondral interface τ slightly decreased from 0.12 to 0.08 with distance (from 1 to 4 μm).

3.5. Quantifying the anisotropy behaviour of permeability

Using the numerical fluid flow modelling, we found a permeability value of 1.9×10^{-23} m^2 perpendicular to osteochondral interface within the connected region (0.7 μm). The fraction of the domain occupied by the disconnected pores hinders the fluid motion, indicative of anisotropic matrix permeability. The anisotropic permeability found here is attributed to the non-uniform orientation of collagen fibrils in the calcified cartilage region (Khanarian et al., 2014). Therefore, permeability predominantly facilitates convective solute and fluid transport in short ranges to the passages where non-calcified cartilage directly touches the subchondral bone plate.

Permeability showed an anisotropic behaviour with values of 3.9×10^{-19} m^2 and 3.2×10^{-20} m^2, parallel and perpendicular to osteochondral interface, respectively. This study provides the first pore-scale reported permeability based on the real subchondral bone plate pericellular architecture at the nano-scale. Notably, our obtained values lie in the range of the previously reported values, see Table 2 (Beno et al., 2006). Perpendicular to osteochondral interface, the permeability of the subchondral bone plate was 1000-fold higher compared to the overlaying calcified cartilage. The range of permeability's of a region involving the bone canalicular region in the present study agrees with that of the previous study based on analytical approaches (Beno et al., 2006). Obviously, larger permeability's were expected when incorporating the contribution of lacunae and vessels.

3.6. The importance of pore size variability

Microscopic pores with different sizes manifest their effect through bulk parameters of diffusivity and permeability. To explore the importance of pore size variability we have performed simulations on the pore structure, once using the real variable pore sizes and once using a single size for all pores (with the value equal to the average value of the real pore sizes). Doing so, solute showed slower penetration into the subchondral bone plate with the real pore size distribution compared to the bone with uniform pore sizes (Fig. 4B). This analysis indicated the contribution of insulated, or dead-end, pore clusters (shown by the dotted circle in Fig. 4B) located along the passage of solutes which act as a sink for the solute to delay its penetration and therefor its arrival at the longer distances. A later arrival at the pore scale, in turn, manifests itself as a smaller effective diffusion value for the bone sample.

The domain with real pore sizes showed 89% higher permeability value compared to its corresponding uniform media. Such a difference indicates the presence of a distinctive pathway (i.e., a series of connected pores which also have larger sizes compared to the rest of the pore matrix). Analysing the pore sizes and their connectivity, the real sample indeed has a pore size distribution where larger pores are spatially correlated and construct a main branch dominating the flow (as shown in Fig. 4B). Therefore, trans-

Table 1
A comparison of the diffusivity values reported in the literature for calcified cartilage and subchondral bone plate.

Research	Tissue origin	Solute	Measurement technique	Diffusivity (m^2/s)
Current	Human	Small (1.5 kDa)	FIB-SEM based Poreflow modelling	CC (parallel to OI): 32.5 to 40 $\times 10^{-12}$ SB (Parallel to OI): 52.5 $\times 10^{-12}$ CC (Perpendicular to OI): 12.5 $\times 10^{-12}$ SB (Perpendicular to OI): 20 to 29.8 $\times 10^{-12}$
Pouran, B., et al. 2016 & Arbabi, V., et al. 2016	Human & Horse	Small (1.5 kDa)	Micro-CT based finite element method	SB/CC (human): 0.95 to 1.72 $\times 10^{-12}$ SB/CC (horse): 0.09 to 0.9 $\times 10^{-12}$
Pan, J., et al., 2012	Mouse	Small (0.4 kDa)	Fluorescence loss induced by photobleaching	Aged group: CC: (0.30 ± 0.17) $\times 10^{-12}$ Between CC & SB: (0.12 ± 0.04) $\times 10^{-12}$ DMM OA group: CC: (0.33 ± 0.20) $\times 10^{-12}$ Between CC & SB: (0.07 ± 0.03) $\times 10^{-12}$
Pan, J., et al., 2009	Mouse	Small (0.4 kDa)	Fluorescence loss induced by photobleaching	CC: (0.26 ± 0.22) $\times 10^{-12}$ Between CC & SB: (0.07 ± 0.03) $\times 10^{-12}$

CC: calcified cartilage
SB: subchondral bone
OI: osteochondral interface
DMM: destabilization of medial meniscus
OA: osteoarthritis

Table 2
A comparison of the permeability values reported in the literature for subchondral bone plate.

Research	Tissue origin	Measurement technique	Permeability (m^2)
Current	Human	FIB-SEM based PoreFlow modelling	Parallel to OI: 3.9×10^{-19} Perpendicular to OI: 3.2×10^{-20}
Beno, T., et al., 2006	Multiple	Analytical	Human: Average: 0.47×10^{-20}

port in the subchondral bone plate is not only affected by the presence of the larger pore sizes (i.e., geometrical properties of the bone) but is also highly controlled by the connectivity pattern between the pores (i.e., a topological property of the bone) and the pore size correlation. Another major conclusion using Fig. 4 is that a bone with higher permeability values does not necessarily have a larger diffusivity – as is the case here. This is because pathways of conductive pores with their larger sizes control bone permeability, while the presence of isolated pore clusters branching out from such a pathway regulates the effective diffusivity. The larger pores in the subchondral bone plate are believed to be the osteocyte processes as opposed to the smaller pores that are formed due to partial mineralization of the collagen fibrils.

4. Conclusion

The results of the present study shed light on the topographic features at the primary interface between articular cartilage and subchondral bone plate and a robust derivation of transport parameters based on the fundamental underlying pore structures. This study considered solute and fluid transport in the porous structure of calcified cartilage, as well as the subchondral bone in the absence of mechanical loading. It is well anticipated that fluid flow associated with loading can remarkably affect transport mechanisms and mechanical responses (Mow et al., 1984; Torzilli et al., 1983). Therefore, it is important to keep this limitation in mind when using the results of the current study when the mechanical loading effects are expected to be significant. Moreover, we recommend that future studies investigate load-dependent transport at the pore scale using the tools presented here. As opposed to the conventional and strict separation between non-calcified and calcified cartilage as well as calcified cartilage and subchondral bone plate, we have shown a nano-scale continuous and transitional architectural pattern across the boundaries. Applying a combination of advanced FIB-SEM tomography and pore-network modelling enabled accurate prediction of the solute and fluid transport properties and their variability in both calcified cartilage and subchondral bone plate. These techniques applied at pore-scale within the extracellular matrix, are believed to make a major step forward in the quantification of mass and momentum transport at the interface of the cartilage and the bone.

Declaration of Competing Interest

The authors declare that they have no known competing financial interests or personal relationships that could have appeared to influence the work reported in this paper.

Acknowledgments

Amir Raoof is a member of Structures of Strength interdisciplinary platform in the Centre for Unusual Collaborations at Utrecht University.

Appendix A. Supplementary data

Supplementary data to this article can be found online at https://doi.org/10.1016/j.jbiomech.2021.110504.

References

Arbabi, V., Pouran, B., Weinans, H., Zadpoor, A.A., 2016a. Multiphasic modeling of charged solute transport across articular cartilage: Application of multi-zone finite-bath model. J. Biomech. 49, 1510–1517.
Arbabi, V., Pouran, B., Weinans, H., Zadpoor, A.A., 2016b. Neutral solute transport across osteochondral interface: A finite element approach. J. Biomech. 49, 3833–3839.
Arbabi, V., Pouran, B., Zadpoor, A.A., Weinans, H., 2017. An Experimental and Finite Element Protocol to Investigate the Transport of Neutral and Charged Solutes across Articular Cartilage. J Vis Exp.
Bajpayee, A.G., Wong, C.R., Bawendi, M.G., Frank, E.H., Grodzinsky, A.J., 2014. Avidin as a model for charge driven transport into cartilage and drug delivery for treating early stage post-traumatic osteoarthritis. Biomaterials 35, 538–549.

Benalla, M., Palacio-Mancheno, P.E., Fritton, S.P., Cardoso, L., Cowin, S.C., 2014. Dynamic permeability of the lacunar-canalicular system in human cortical bone. Biomech. Model. Mechanobiol. 13, 801–812.
Beno, T., Yoon, Y.J., Cowin, S.C., Fritton, S.P., 2006. Estimation of bone permeability using accurate microstructural measurements. J. Biomech. 39, 2378–2387.
Burstein, D., Velyvis, J., Scott, K.T., Stock, K.W., Kim, Y.J., Jaramillo, D., Boutin, R.D., Gray, M.L., 2001. Protocol issues for delayed Gd(DTPA)(2-)-enhanced MRI (dGEMRIC) for clinical evaluation of articular cartilage. Magn. Reson. Med. 45, 36–41.
Chin, H.C., Moeini, M., Quinn, T.M., 2013. Solute transport across the articular surface of injured cartilage. Arch. Biochem. Biophys. 535, 241–247.
de Winter, D.A., Meirer, F., Weckhuysen, B.M., 2016. FIB-SEM Tomography Probes the Mesoscale Pore Space of an Individual Catalytic Cracking Particle. ACS Catal. 6, 3158–3167.
Fan, L., Pei, S., Lucas Lu, X., Wang, L., 2016. A multiscale 3D finite element analysis of fluid/solute transport in mechanically loaded bone. Bone Res. 4, 16032.
Hughes, L.C., Archer, C.W., ap Gwynn, I., 2005. The ultrastructure of mouse articular cartilage: collagen orientation and implications for tissue functionality. A polarised light and scanning electron microscope study and review. Eur. Cell Mater. 9, 68-84.
Khanarian, N.T., Boushell, M.K., Spalazzi, J.P., Pleshko, N., Boskey, A.L., Lu, H.H., 2014. FTIR-I compositional mapping of the cartilage-to-bone interface as a function of tissue region and age. J. Bone Miner. Res. 29, 2643–2652.
Leddy, H.A., Guilak, F., 2003. Site-Specific Molecular Diffusion in Articular Cartilage Measured using Fluorescence Recovery after Photobleaching. Ann. Biomed. Eng. 31, 753–760.
Lyons, T.J., McClure, S.F., Stoddart, R.W., McClure, J., 2006. The normal human chondro-osseous junctional region: evidence for contact of uncalcified cartilage with subchondral bone and marrow spaces. BMC Musculoskelet Disord. 7, 52.
Mahmoodlu, M.G., Raoof, A., Bultreys, T., Van Stappen, J., Cnudde, V., 2020. Large-scale pore network and continuum simulations of solute longitudinal dispersivity of a saturated sand column. Adv. Water Resour. 144, 103713.
Mahmoodlu, M.G., Raoof, A., Sweijen, T., van Genuchten, M.T., 2016. Effects of Sand Compaction and Mixing on Pore Structure and the Unsaturated Soil Hydraulic Properties. Vadose Zone J. 15.
Mow, V.C., Holmes, M.H., Lai, W.M., 1984. Fluid transport and mechanical properties of articular cartilage: a review. J. Biomech. 17, 377–394.
Narayan, K., Subramaniam, S., 2015. Focused ion beams in biology. Nat. Methods 12, 1021–1031.
Pan, J., Wang, B., Li, W., Zhou, X., Scherr, T., Yang, Y., Price, C., Wang, L., 2012. Elevated cross-talk between subchondral bone and cartilage in osteoarthritic joints. Bone 51, 212–217.
Pan, J., Zhou, X., Li, W., Novotny, J.E., Doty, S.B., Wang, L., 2009. In situ measurement of transport between subchondral bone and articular cartilage. J. Orthopaedic Res.: Offic. Publ. Orthopaedic Res. Soc. 27, 1347–1352.
Pouran, B., Arbabi, V., Bajpayee, A.G., van Tiel, J., Toyras, J., Jurvelin, J.S., Malda, J., Zadpoor, A.A., Weinans, H., 2018. Multi-scale imaging techniques to investigate solute transport across articular cartilage. J. Biomech. 78, 10–20.
Pouran, B., Arbabi, V., Bleys, R.L., Rene van Weeren, P., Zadpoor, A.A., Weinans, H., 2016a. Solute transport at the interface of cartilage and subchondral bone plate: Effect of micro-architecture. J. Biomech.
Pouran, B., Arbabi, V., Zadpoor, A.A., Weinans, H., 2016b. Isolated effects of external bath osmolality, solute concentration, and electrical charge on solute transport across articular cartilage. Med. Eng. Phys. 38, 1399–1407.
Quinn, T.M., Morel, V., Meister, J.J., 2001. Static compression of articular cartilage can reduce solute diffusivity and partitioning: implications for the chondrocyte biological response. J. Biomech. 34, 1463–1469.
Raoof, A., Nick, H.M., Hassanizadeh, S.M., Spiers, C.J., 2013. PoreFlow: A complex pore-network model for simulation of reactive transport in variably saturated porous media. Comput. Geosci. 61, 160–174.
Sophia Fox, A.J., Bedi, A., Rodeo, S.A., 2009. The Basic Science of Articular Cartilage: Structure, Composition, and Function. Sports Health 1, 461–468.
Torzilli, P.A., Adams, T.C., Mis, R.J., 1987. Transient solute diffusion in articular cartilage. J. Biomech. 20, 203–214.
Torzilli, P.A., Dethmers, D.A., Rose, D.E., Schryuer, H.F., 1983. Movement of interstitial water through loaded articular cartilage. J. Biomech. 16, 169–179.
Wang, L., Cowin, S.C., Weinbaum, S., Fritton, S.P., 2000. Modeling tracer transport in an osteon under cyclic loading. Ann. Biomed. Eng. 28, 1200–1209.
Weinans, H., Siebelt, M., Agricola, R., Botter, S.M., Piscaer, T.M., Waarsing, J.H., 2012. Pathophysiology of peri-articular bone changes in osteoarthritis. Bone 51, 190–196.
Winter, D.A.M.D., Schneijdenberg, C.T.W.M., Lebbink, M.N., Lich, B., Verkleij, A.J., Drury, M.R., Humbel, B.M., 2009. Tomography of insulating biological and geological materials using focused ion beam (FIB) sectioning and low-kV BSE imaging. J. Microsc. 233, 372–383.